REGULAR ARTICLE

Theoretical study on the working mechanism of a reversible light-driven rotary molecular motor

**Lili Wang · Xin Che · Huiliang Li ·
Jun Gao · Chengbu Liu**

Abstract Recent progress in the experimental design and synthesis of artificial light-driven molecular motors has made it possible to reverse the light-powered rotation of a molecular motor during the rotary process with multilevel control of rotary motion. With the interconversion between the photochemically generated less-stable isomers in one unidirectional rotary cycle with the stable isomers in the other cycle, the clockwise and anticlockwise rotations can be regulated with configuration inversion at the stereogenic centre. In this work, we report theoretical calculations by using density functional theory and time-dependent density functional theory, revealing the working mechanism of the clockwise and anticlockwise rotations. Specifically, by locating the relevant stationary points along the excited-state and ground-state reaction paths, the clockwise and anticlockwise rotary cycles are explored in great detail, which is of complementary importance in understanding the overall rotary process of the reversible rotation.

Dedicated to Professor Guosen Yan and published as part of the special collection of articles celebrating his 85th birthday.

Electronic supplementary material The online version of this article (doi:10.1007/s00214-014-1566-6) contains supplementary material, which is available to authorized users.

L. Wang
Advanced Research Center for Optics, Shandong University, Jinan 250100, People's Republic of China

L. Wang · X. Che · H. Li · J. Gao (✉) · C. Liu
School of Chemistry and Chemical Engineering, Shandong University, Jinan 250100, People's Republic of China
e-mail: gaojun@sdu.edu.cn

L. Wang
State Key Laboratories of Transducer Technology, Shanghai Institute of Microsystem and Information Technology, Chinese Academy of Sciences, Shanghai 200050, People's Republic of China

1 Introduction

Molecular motor, in general, is a kind a nano-machine which can perform continuously mechanical functions by converting external energy to repetitive 360° motion. There are various molecular motors in nature, existing in the biological systems such as ATPase, dimeric kinesin, myosin, and dynein, which accomplish the extremely delicate and intricate microscopic works that compose the brilliant biological world. According to the different driven forces, it can be sorted as chemical [1], electrical, thermal, and light-driven molecular motors. On the other hand, due to the rapid development of the 'bottom-up' approach for experimental chemists, studies focusing on the design and synthesis of molecular-level machines that mimic the basic functions in nature have increased dramatically in the past decade. Although it is still far to construct artificial molecular motor that can perform integrated functions for realistic works, people have been able to design and to synthesis some relatively simple molecular motors which possess linear or rotary movement working under ambient conditions.

An eligible biological or artificial molecular motor that can be operated effectively at molecular level should work against the random thermal Brownian motion, which means the unidirectionality and controllability of the motor are essential criteria. The artificially designed molecular motors in laboratory that are powered by different energy sources and possess various mechanical motions have been

inspired extensively by the pioneering synthetic unidirectional rotary molecular motors presented by Feringa [2, 3] and Kelly [4, 5] and their co-workers over the last 15 years.

One of the most interesting characteristics of the rotary motors existing in biological systems is the reversal of the direction of rotation [6]. Recently, a new molecular motor (henceforth denoted motor **1**) driven by light, whose rotation direction can be controlled to be capable of performing reversible mechanical works by certain chemical catalysis epimerization, has been reported by Feringa et al. [7]. The design of motor **1** is based on one of the typical second-generation molecular motor (shown in Scheme 1) by replacing the methyl substituent at the stereogenic centre 2′ position with electron-withdrawing—CONMe₂ group at the 3′ position [7, 8]. In this way, the bidirectional 360° rotary cycle of motor **1** can be achieved, and the concerted working mechanism was experimentally observed, as shown in Fig. 1. According to the relative rotating between the upper rotor and lower stator, the two rotating cycles are named *clockwise* rotation and *anticlockwise* rotation, respectively.

Computational studies complement these experimental efforts and provide more insights into the rationale of the working mechanism, which could be helpful for the design and operation of these high rotational frequency motors in functional devices [9–12]. Moreover, quantum chemical studies could be regarded as the first step before exploring the rotary cycle of such motors by making them work as practical molecular machines. Some theoretical studies focusing on the working mechanisms of different light-driven molecular motors have been reported widely. Grimm et al. [13] have investigated the photochemical steps of a Feringa alkene-based molecular motor by using Car–Parrinello molecular dynamics simulations and thermal steps by semiempirical AM1 method, which has revealed the important role of methyl groups in determining the unidirectionality of the rotation. Excited-state dynamics studies of fluorene-based molecular motor also include TD-DFT simulation [14] and semiclassical trajectory surface hopping (TSH) simulations combined with orthogonalization-corrected OM2 Hamiltonian and multireference configuration interaction treatment (OM2/MRCI) by Filatov et al. [15]. Recently, the detailed photoisomerization processes of a redesigned stilbene-based light-driven molecular motor were specified by Liu and Morokuma [16] with CASPT2//CASSCF calculations. On the contrary, Perez-Hernandez and González [17] mainly focused on the possible reaction paths and corresponding transition states in the ground state.

As for the working mechanism of motor **1**, despite the experimental observation has shown the bidirectional rotations, a detailed understanding of the excited-state photoisomerization and ground-state thermal helix inversion following the rotary motion is still of essential importance
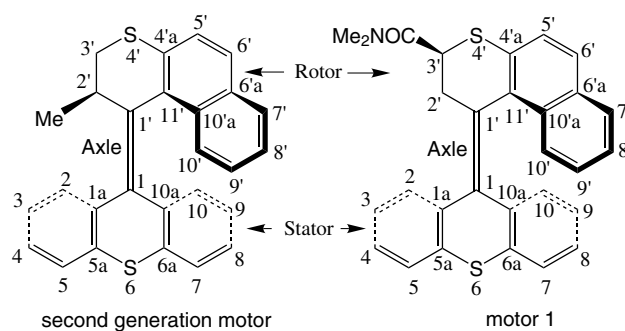

Scheme 1 Second-generation (*left panel*) and redesigned reversible rotary motor **1** (*right panel*). With dihedral angles defined as follows, $\theta = $ C11′–C1′–C1–C10a, $\alpha = $ C1–C1′–C11′–C10′a, $\alpha' = $ C1′–C1–C10a–C10, $\beta = $ C1–C1′–C2′–C3′, and $\beta' = $ C1′–C1–C1a–C2

considering improved design of reversible light-driven rotary molecular motors in the future.

We report quantum chemical calculations in this work by using density functional theory (DFT) [18–24] and time-dependent density functional theory (TD-DFT) [25–29], which illustrate the overall rotary process including both the excited-state photoisomerization and the ground-state thermal helix inversion steps at the same level of theory. It is found that the long-range corrected (LC) density functional CAM-B3LYP [30] is able to demonstrate the unidirectionality of the photoisomerizations in the *clockwise* and *anticlockwise* rotary processes. By computing the potential energy curves (PECs) of the ground state and three lowest excited states, the different profiles of these states in the power-stroke photochemical reactions have been revealed.

2 Computational methods

The complete understanding of the rotary cycle of motor **1** involves the description of both photoisomerization reaction and thermal helix inversion steps. Therefore, the selection of a rational computational method that is equally good at describing excited-state and ground-state potential energy surfaces at the same level of theory is of fundamental importance. Although the widely used globally hybrid density functional B3LYP [18, 21, 31] is recognized as one of the most accurate for ground-state structures, energies, and frequencies [18, 21], there are still some limitations for handling partial π-bond breaking or interactions dominated by medium-range correlation energy such as overestimate of rotation barriers [32], failure to give correct excitation energies [33–35], and shortcomings in some other cases [36]. Hence, CAM-B3LYP was employed in the work motivated by its merit in describing the excited-state potential energy surfaces as well as relatively accurate ground-state energy barriers as demonstrated by Rostov et al. [34, 35].
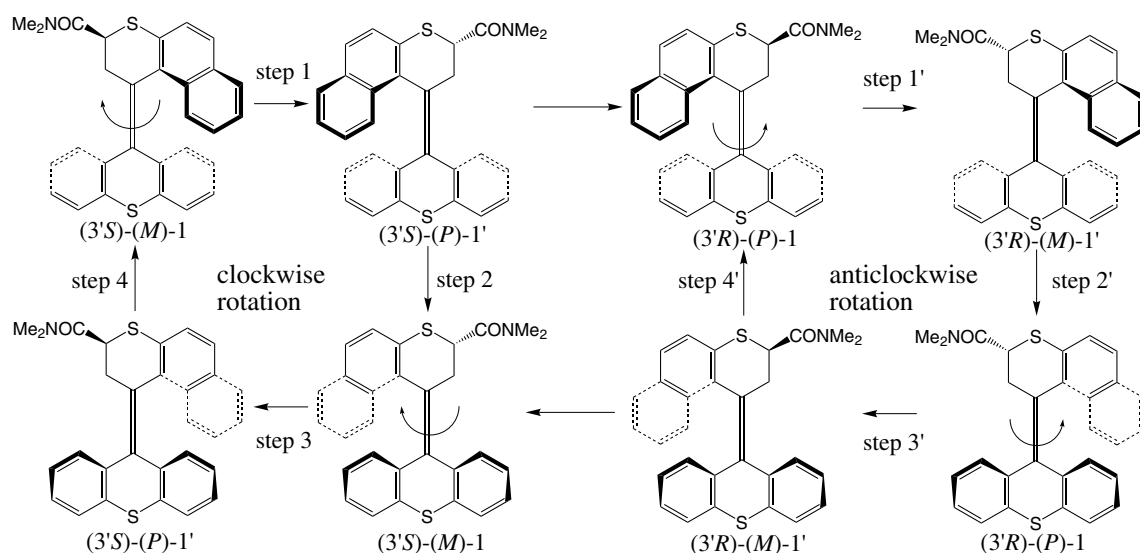
Fig. 1 Schematic *clockwise* and *anticlockwise* rotary cycles of motor **1**

Table 1 CAM-B3LYP and B3LYP ground-state geometric parameters and relative energetic differences of two most stable structures (3′S)-(M)-1 and (3′R)-(P)-1 with different basis sets

Isomer	Method	Basis set	θ	α	α'	β	β'	C1′–C1	ΔG
(3′S)-(M)-1	CAM-B3LYP	6−31G+(d,p)	0.2 (177.3)	−63.4	−50.5	−107.1	52.4	1.348	0.0
		6−311G++(d,p)	0.5 (177.3)	−63.6	−51.0	−107.2	52.9	1.343	0.0
	B3LYP	6−31G+(d,p)	−0.9 (176.5)	−63.1	−49.9	−107.0	51.7	1.359	0.2
		6−311G++(d,p)	−0.6 (176.7)	−63.4	−50.4	−107.1	52.2	1.354	0.2
(3′R)-(P)-1)	CAM-B3LYP	6−31G+(d,p)	−177.2 (−0.2)	63.5	50.4	107.0	−52.5	1.348	0.0
		6−311G++(d,p)	−177.3 (−0.5)	63.6	51.0	107.2	−52.9	1.343	0.0
	B3LYP	6−31G+(d,p)	−176.3 (1.1)	63.0	50.0	106.6	−51.9	1.359	0.0
		6−311G++(d,p)	−176.4 (0.7)	63.4	50.6	106.7	−52.5	1.354	0.0

The definition of dihedral angles is listed in Scheme 1. Dihedral angles in degrees, bond lengths in angstrom, and relative energies in kJ mol^{-1}. ΔG is the relative energy differences between (3′S)-(M)-1 and (3′R)-(P)-1 computed at the same level of theory

In order to explore the rotary cycle of motor 1 with clarity and simplicity, each 360° rotation process of *clockwise* and *anticlockwise* is divided into two identical rotary halves due to the symmetric chemical structure of the lower stator, i.e., every 180° half includes a photochemical and a thermal step (step 1 and step 2 for *clockwise* rotation and step 1′ and step 2′ for *anticlockwise* rotation as shown in Fig. 1). The two most stable stationary points ((3′S)-(M)-1 and (3′R)-(P)-1) on the ground state were located by geometry optimizations and frequency calculations using long-range corrected hybrid density functional CAM-B3LYP in combination with the 6−31+G(d,p) basis set. As a complementary comparison, geometry optimizations and frequency calculations with B3LYP functional and 6−31+G(d,p) basis set were also performed to ensure the reliability of CAM-B3LYP for ground-state properties (see Table 1 in following section).

Starting from (3′S)-(M)-1 and (3′R)-(P)-1 as the most stable structures on the ground state in each rotary cycle, constrained geometry optimizations along the dihedral angle C11′–C1′–C1–C10a (θ in Table 1) with an interval of 10° were carried out with the same DFT methodology to identify the ground-state PECs. Then, based on the ground-state minima and PECs, the excited-state PECs in each rotary cycle ((3′S)-(P)-1′ and (3′R)-(M)-1′) including the three lowest electronic excited states (S$_1$, S$_2$, and S$_3$) were evaluated by TD-DFT single-point calculations at CAM-B3LYP/6−311++G(d,p) level of theory, where triple-ζ quality and more diffuse functions are included (basis set effect on the ground-state geometries also discussed in Table 1). It should be noticed that during the Franck–Condon (FC) relaxation, i.e. analytic TD-DFT gradients [28, 37] calculations from (3′S)-(M)-1 and (3′R)-(P)-1 structures, 6−31+G(d,p) basis set and

Tamm–Dancoff approximation (TDA) [38] were employed in order to give balanced results between accuracy and efficiency. Afterwards, TD-DFT single-point excitation energies of the TDA optimized geometries were calculated at 311++G(d,p) level.

The less-stable structures $(3'S)$-(P)-1 and $(3'R)$-(M)-1 can be recognized as products of photoisomerizations, whereafter the transition state search was carried out by constrained geometry optimization along the relevant dihedral angle α shown in Scheme 1. The saddle-point structure for each curve was taken out and was optimized to a transition structure at B3LYP/6−31G+(d,p) level of theory using the standard transition state search algorithms implemented in Gaussian 09 [39]. After a transition structure is optimized, the geometries and energies were refined using B3LYP/6−311G++(d,p) and CAM-B3LYP/6−311G++(d,p) together with the frequency calculations in order to confirm all the transition structures have only one imaginary frequency and to obtain thermal corrected free energies. Also, intrinsic reaction coordinate calculations were done to make sure the reactants and products do connected by a given transition structure.

All calculations in this work were performed with Gaussian 09 package of programs [39].

3 Results and discussions

3.1 The $(3'S)$-(P)-1 and $(3'R)$-(M)-1 isomers

Taken as the preliminary photochemical reactants in each rotary cycle, the ground-state geometric parameters and relative energy difference of $(3'S)$-(M)-1 and $(3'R)$-(P)-1 were computed by CAM-B3LYP and B3LYP with different basis sets, respectively, as shown in Table 1.

It can be known from Fig. 1 the stable mirror opposite enantiomer $(3'R)$-(P)-1 which can be obtained by base-catalysed epimerization of the less-stable $(3'S)$-(P)-1' should be of the same stereogenic structure and energetic stability with $(3'S)$-(M)-1. It is confirmed by

the comparison in Table 1, in which the maximum disparities are 0.1°, 0.0 Å, and 0.0 kJ mol^{-1} for CAM-B3LYP/6−31G+(d,p), 0.0°, 0.0 Å, and 0.0 kJ mol^{-1} for CAM-B3LYP/6−311G++(d,p), 0.4°, 0.0 Å, and 0.2 kJ mol^{-1} for B3LYP/6−31G+(d,p), and 0.4°, 0.0 Å, and 0.2 kJ mol^{-1} for B3LYP/6−311G++(d,p) in dihedral angles, C1'–C1 bonds, and relative energies. Moreover, the increase in the size of the basis set from 6−31G+(d,p) to 6−311G++(d,p) has similar and minor effect on the chemical structures, with maximum disparities of 0.5° and 0.005 Å for CAM-B3LYP, and 0.6° and 0.005 Å for B3LYP.

From this point of view, both functionals combined with each of two basis sets give reasonably good description of the ground-state geometry and energy. Importantly, CAM-B3LYP predicts $(3'S)$-(M)-1 and $(3'R)$-(P)-1 to be exactly identical, which proves that this functional is capable of yielding accurate ground-state results needed for the calculations in this work.

3.2 FC relaxation and potential energy curves

As the first power stroke in the rotary cycle, the irradiation of light promotes the two initial structures in each cycle, $(3'S)$-(M)-1 and $(3'R)$-(P)-1, to the higher energy excited electronic states, followed by an ultrafast relaxation to the S_1 minimum region, which can be evidenced by the electronic structure analyses for the three lowest electronic excited states. (For detailed discussion, please refer to the Supporting Information.) The energy difference between vertical and adiabatic excitation energy is the driving force of the photoisomerization process, and the isomer is considered to go down to the ground state near the twisted perpendicular conical intersection. Therefore, the directionality of the photoinitiated rotation around C1'–C1 is controlled by the FC relaxation and can be reflected by the shape of PECs on the excited state. Some key parameters of excitation energy and geometry variation during this process are collected and shown in Table 2.

Table 2 S_1 vertical (VEE) and adiabatic (AEE) excitation energies (eV) of $(3'S)$-(M)-1 and $(3'R)$-(P)-1 calculated at CAM-B3LYP with 6−31G+(d,p) and 6−311G++(d,p) level of theory

Isomer	Basis set	λ_{max}^{b}	VEE	AEE	Geometry change	
					$\Delta\theta$	ΔC1'–C1
$(3'S)$-(M)-1	6−31G+(d,p)	3.97	4.14	2.99	$0.2 \rightarrow -57.5$	$1.348 \rightarrow 1.447$
	6−311G++(d,p)^a		4.14	3.01	–	–
$(3'R)$-(P)-1	6−31G+(d,p)	3.97	4.14	2.99	$-177.2 \rightarrow -126.4$	$1.348 \rightarrow 1.447$
	6−311G++(d,p)^a		4.14	3.01	–	–

[a] The excitation energies are computed from the geometries optimized with 6−31G+(d,p) basis set

[b] Experimental absorption maximum taken from Ref. [7]

It can be seen from Table 2 how well CAM-B3LYP can describe the excitation energies of the excited electronic states. The vertical excitation energies (∼0.15 eV higher than the experimental values) are in reasonable agreement with the experimental absorption maxima which should correspond to the vertical approximation, as the calculated adiabatic excitation energies are ∼0.90 eV lower than the experimental values. The basis set effect was evaluated by single-point calculations increasing basis set from 6−31G+(d,p) to 6−311G++(d,p) and only shows marginal difference (∼0.02 eV in adiabatic excitation energies). With regard to the geometry changes during the FC relaxation of the two isomers, there are both similarity and difference. While a pronounced elongation of ∼0.1 Å in C1′–C1 bond is observed for both isomers, the driving forces on the relative rotation between rotor and stator of (3′S)-(M)-1 and (3′R)-(P)-1 are of opposite directions which can be observed clearly in Fig. 2.

In Fig. 2, the S_0 minimum energy path (MEP) and the single-point excitation energies of the first three excited states for (3′S)-(M)-1 and (3′R)-(P)-1 are shown. It should be pointed out that the aim of the research is to elucidate the reversible rotation processes and to understand the working mechanism of the motor; therefore, the expensive excited-state potential energy surface calculation was not performed. Furthermore, although CAM-B3LYP functional performs well for the excitation energy calculation, it is a single-reference method and is well known not as good as multireference methods in describing conical intersections. Instead, the nature of the excited-states MEPs was estimated by computing the single-point excitation energies of the first three excited states from the optimized geometries on S_0 MEP, and still some interesting features are revealed.

As shown in Fig. 2, the key feature is the inversion symmetry of the PECs of the two isomers. As for the (3′S)-(M)-1 isomer, the FC relaxation on the excited state follows the S_1 PEC after the molecule is excited, which results from the barrierless feature of the first excited state and high energy barriers on the second and third excited states.

The descent of energy from the FC point on the S_1 PEC drives the excited state isomerization towards the twisted intermediate conformation (3′S)-(M)-1*. The dihedral angle θ changes from ∼0° to −60° roughly, suggesting an efficient *clockwise* initial rotation. While for the (3′R)-(P)-1 isomer, the PECs feature similar characteristics with that of the (3′S)-(M)-1 isomer, except the dihedral angle θ changes from ∼−180° to ∼−120° towards (3′R)-(P)-1* and is in an *anticlockwise* fashion.

As indicated in the discussion above, both S_1 and S_0 PECs in Fig. 2 cannot be capable of locating the conical intersections between the excited state and ground state. Nevertheless, an excitation energy of approximately zero is shown at −130° for (3′S)-(M)-1 and at −50° for (3′R)-(P)-1, which indicates that the conical intersection is in the range of (−60°, −130°) for (3′S)-(M)-1 and (−120°, −50°) for (3′R)-(P)-1, respectively. Such assumption can be further confirmed by carrying out ground-state geometry optimizations from twisted (3′S)-(M)-1* and (3′R)-(P)-1* conformations to locate the less-stable photochemical products. Interestingly, it was observed that in the intermediate (3′S)-(M)-1* and (3′R)-(P)-1* conformations, the orientation of phenyl rings on the stator has changed from pointing-in the plane to pointing-out direction. Furthermore, when optimized to the ground-state minima from the excited-state intermediates (3′S)-(M)-1* and (3′R)-(P)-1*, the orientation of phenyl rings on the stator was preserved and less-stable structures (named as (3′S)-(P)-1 and (3′R)-(M)-1) different with that in the original working mechanism (shown in Fig. 1) were obtained. The photochemical products (3′S)-(P)-1 and (3′R)-(M)-1 suggest that motor 1 should work in a slightly different manner that does lead to the experimentally observed thermal barriers.

3.3 Working cycles and transition states

Taken as the rate-determining steps in the overall rotary cycle, the thermal helix inversions of step 2 and step 2′ start from the photoisomerized (3′S)-(P)-1 in the clockwise

Fig. 2 FC relaxation directions and excitation energies with S_0 MEPs for (3′S)-(M)-1 (*left panel*) and (3′R)-(P)-1 (*right panel*). The photoisomerization directions indicated by *green arrows*
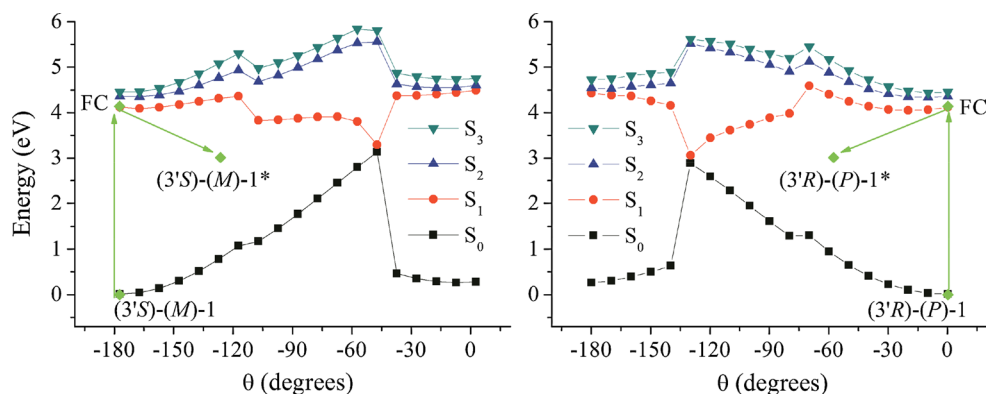
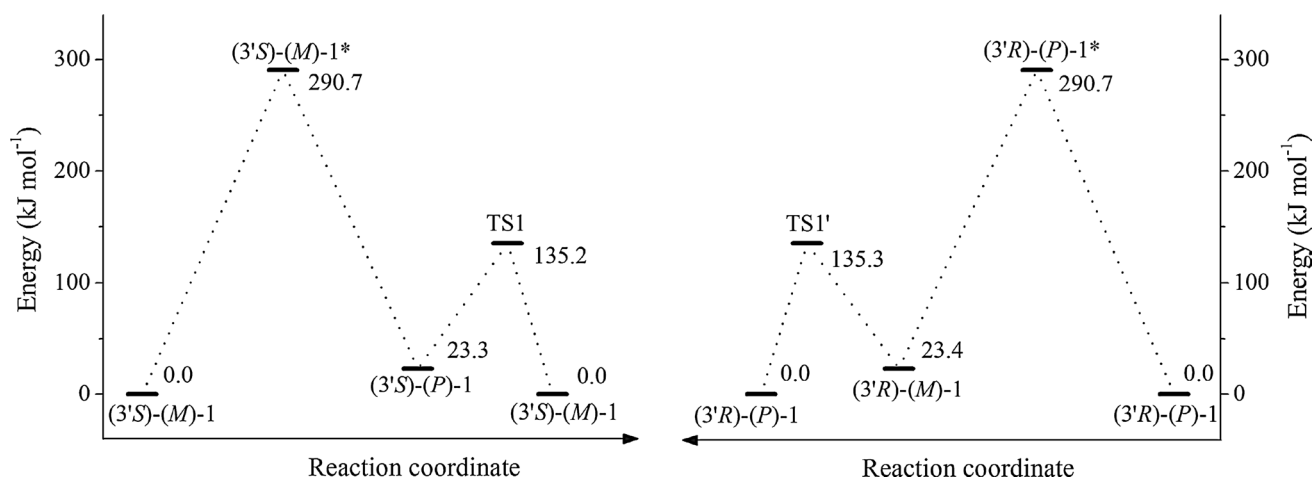rotation and from (3′R)-(M)-1 in the anticlockwise rotation, during the first half of each rotary cycle. The location of transition states is of utmost importance in determining the rotary frequency and in understanding the working mechanism of the motor. To this aim, two-dimensional relaxed potential energy scans are carried out by changing torsional angle α and α' in order to get suitable starting geometries for the geometry optimizations of transition states. After the corresponding transition states are optimized, all of the requisite frequency and intrinsic reaction coordinate calculations are performed to get the free energies and to verify the reactants and products mediated by the transition states. (The atomic coordinates of optimized ground and excited-state stationary points are provided in Supporting Information.) By means of locating all the possible stationary

points, the proposed feasible working cycles for the clockwise and anticlockwise rotations are shown in Fig. 3. The exclusive *syn-fold* structures (3′S)-(P)-1 and (3′R)-(M)-1 of the photochemical products have been theoretically predicted, which means that there is an *anti-fold → syn-fold* geometrical transformation during the rotary process. All the five isomers of motor 1 in step 1 and step 2 of clockwise rotation and another five isomers in step 1′ and step 2′ are depicted in Fig. 4, where also given are the relative stabilities of different isomers with respect to the *global* stable isomer in each rotary cycle.

As shown clearly in Fig. 4, the clockwise and anticlockwise rotary cycles show highly symmetric characteristic, which has an opposite rotary direction but nearly equivalent relative free energies for all the corresponding isomers
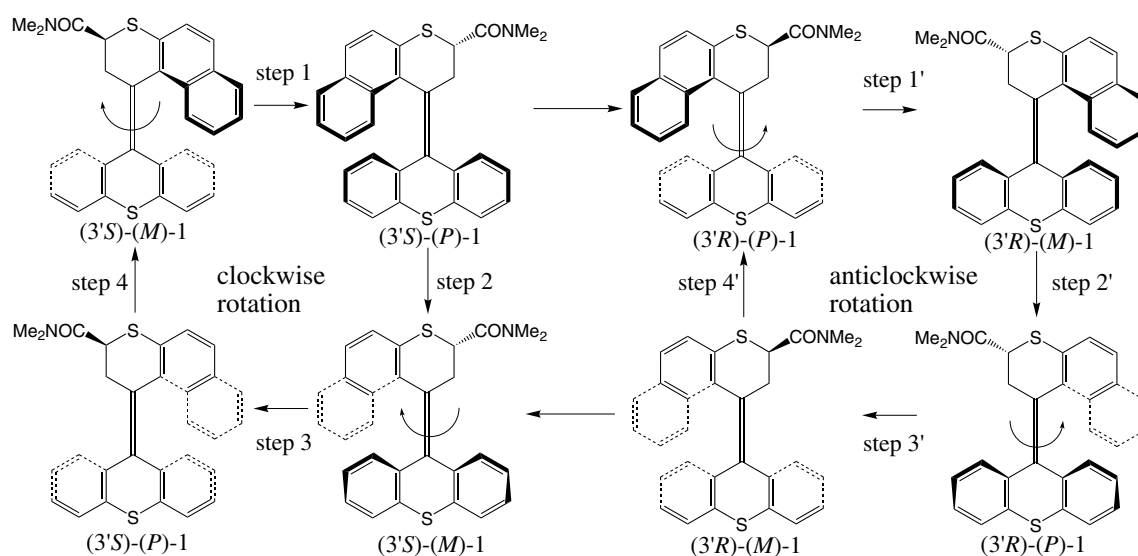
Fig. 3 Proposed feasible working cycles for the *clockwise* and *anticlockwise* rotations

Fig. 4 Relative free energies (in kJ mol^{-1}) at CAM-B3LYP/6−31G+(d,p) level of theory with respect to the most stable isomers of motor 1 in the *clockwise* and *anticlockwise* rotations

in each cycle. The step 1 of the clockwise rotation and step 1′ of the anticlockwise rotation are the power stroke photochemical steps, which go through the excited-state intermediates (3′S)-(M)-1* and (3′R)-(P)-1*, respectively. The subsequent concerted thermal helix inversion steps are accomplished via the transition states TS1 and TS1′. The Gibbs free energies for the thermal isomerizations were found experimentally to be 107.9 kJ mol^{-1} for the energetically downhill isomerization and 120.1 kJ mol^{-1} for the uphill isomerization [7]. Accordingly, the obtained activation barriers for the downhill isomerization (from (3′S)-(P)-1 to TS1 for step 2 and from (3′R)-(M)-1 to TS1′ for step 2′) and the uphill isomerization (from (3′S)-(M)-1 to TS1 for step 2 and from (3′R)-(P)-1 to TS1′ for step 2′) are about 111.9 and 135.2 kJ mol^{-1}, which is in good agreement with the experimental ones. Also compared with the experimental results is the temperature effect on the rate constant of the thermal downhill isomerization process which gives the same trend as provided by the experiment (See Supporting Information for more detail).

As for the different photoisomerization products compared with that observed from the experiment, our calculations do predict the *syn-fold* conformers in both clockwise and anticlockwise rotary cycles. Although there is lack of evidence for the existence of *syn-fold* isomers of motor 1, both experimental and theoretical studies have identified the *syn-fold* conformers as possible chemical constitutions for certain second-generation light-driven molecular motors with analogous structure [17, 40].

4 Conclusions

In summary, using long-range corrected density functional CAM-B3LYP, we have explored the working mechanism of a recently synthesized reversible light-driven molecular motor in detail by locating all the stationary points along the reaction paths. The different profiles of the ground-state and three lowest excited-states PECs were evaluated, by which the unidirectional *clockwise* and *anticlockwise* rotary motions of the photoisomerizations can be well understood. Although the appreciable structures of the conical intersections of S_0/S_1 are not accurately located, we are able to obtain the less-stable photochemical products by optimizing the highly twisted molecular structures within a large range to the ground state. Interestingly, the photoisomerization products show *syn-fold* conformations which are slightly different with that in the experiments, for which there are possible evidences both from experimental and theoretical studies of light-driven molecular motors with similar structures. Finally, by comparing the excitation energies and calculated free-energy barriers with the experimental values, it has been found that the

CAM-B3LYP function cannot only give good description of excited states, but also show good performance for the thermal helix reactions.

References

1. Kelly TR, Cai XL, Damkaci F, Panicker SB, Tu B, Bushell SM, Cornella I, Piggott MJ, Salives R, Cavero M, Zhao YJ, Jasmin S (2007) Progress toward a rationally designed, chemically powered rotary molecular motor. J Am Chem Soc 129(2):376–386
2. Harada N, Koumura N, Feringa B (1997) Chemistry of unique chiral olefins. 3. Synthesis and absolute stereochemistry of trans- and cis-1,1′,2,2′,3,3′,4,4′-octahydro-3,3′-dimethyl-4,4′-biphenanthrylidenes. J Am Chem Soc 119(31):7256–7264
3. Koumura N, Zijlstra RWJ, van Delden RA, Harada N, Feringa B (1999) Light-driven monodirectional molecular rotor. Nature 401(6749):152–155
4. Kelly TR, De Silva H, Silva RA (1999) Unidirectional rotary motion in a molecular system. Nature 401(6749):150–152
5. Kelly TR (2001) Progress toward a rationally designed molecular motor. Acc Chem Res 34(6):514–522
6. Henningsen U, Schliwa M (1997) Reversal in the direction of movement of a molecular motor. Nature 389(6646):93–96
7. Ruangsupapichat N, Pollard MM, Harutyunyan SR, Feringa BL (2011) Reversing the direction in a light-driven rotary molecular motor. Nat Chem 3(1):53–60
8. Koumura N, Geertsema EM, van Gelder MB, Meetsma A, Feringa BL (2002) Second generation light-driven molecular motors. Unidirectional rotation controlled by a single stereogenic center with near-perfect photoequilibria and acceleration of the speed of rotation by structural modification. J Am Chem Soc 124(18):5037–5051
9. Amatatsu Y (2011) Theoretical design of a light-driven molecular rotary motor with low energy helical inversion: 9-(5-methyl-2-phenyl-2-cyclopenten-1-ylidene)-9H-fluorene. J Phys Chem A 115(46):13611–13618
10. Amatatsu Y (2012) Theoretical design of a fluorene-based light-driven molecular rotary motor with constant rotation. J Phys Chem A 116(41):10182–10193
11. Fang C, Oruganti B, Durbeej B (2014) Computational study of the working mechanism and rate acceleration of overcrowded alkene-based light-driven rotary molecular motors. RSC Adv 4(20):10240–10251
12. García-Iriepa C, Marazzi M, Zapata F, Valentini A, Sampedro D, Frutos LM (2013) Chiral hydrogen bond environment providing unidirectional rotation in photoactive molecular motors. J Phys Chem Lett 4(9):1389–1396
13. Grimm S, Brauchle C, Frank I (2005) Light-driven unidirectional rotation in a molecule: ROKS simulation. ChemPhysChem 6(9):1943–1947
14. Kazaryan A, Kistemaker JCM, Schäfer LV, Browne WR, Feringa BL, Filatov M (2010) Understanding the dynamics behind the photoisomerization of a light-driven fluorene molecular rotary motor. J Phys Chem A 114(15):5058–5067
15. Kazaryan A, Lan ZG, Schafer LV, Thiel W, Filatov M (2011) Surface hopping excited-state dynamics study of the

photoisomerization of a light-driven fluorene molecular rotary motor. J Chem Theory Comput 7(7):2189–2199

16. Liu F, Morokuma K (2012) Computational study on the working mechanism of a stilbene light-driven molecular rotary motor: sloped minimal energy path and unidirectional nonadiabatic photoisomerization. J Am Chem Soc 134(10):4864–4876

17. Perez-Hernandez G, Gonzalez L (2010) Mechanistic insight into light-driven molecular rotors: a conformational search in chiral overcrowded alkenes by a pseudo-random approach. Phys Chem Chem Phys 12(38):12279–12289

18. Lee CT, Yang WT, Parr RG (1988) Development of the Colle–Salvetti correlation-energy formula into a functional of the electron density. Phys Rev B 37(2):785–789

19. Becke AD (1992) Density-functional thermochemistry. II. The effect of the Perdew–Wang generalized-gradient correlation correction. J Chem Phys 97(12):9173–9177

20. Becke AD (1992) Density-functional thermochemistry. I. The effect of the exchange-only gradient correction. J Chem Phys 96(3):2155–2160

21. Becke AD (1993) Density-functional thermochemistry. III. The role of exact exchange. J Chem Phys 98(7):5648–5652

22. Becke AD (1996) Density-functional thermochemistry. IV. A new dynamical correlation functional and implications for exact-exchange mixing. J Chem Phys 104(3):1040–1046

23. Becke AD (1997) Density-functional thermochemistry. V. Systematic optimization of exchange-correlation functionals. J Chem Phys 107(20):8554–8560

24. Arabi AA, Becke AD (2012) Assessment of the PW86+ PBE+ XDM density functional on van der Waals complexes at non-equilibrium geometries. J Chem Phys 137(1):7

25. Runge E, Gross EKU (1984) Density-functional theory for time-dependent systems. Phys Rev Lett 52(12):997–1000

26. Bauernschmitt R, Ahlrichs R (1996) Treatment of electronic excitations within the adiabatic approximation of time dependent density functional theory. Chem Phys Lett 256(4–5):454–464

27. Casida ME, Jamorski C, Casida KC, Salahub DR (1998) Molecular excitation energies to high-lying bound states from time-dependent density-functional response theory: characterization and correction of the time-dependent local density approximation ionization threshold. J Chem Phys 108(11):4439–4449

28. Furche F, Ahlrichs R (2002) Adiabatic time-dependent density functional methods for excited state properties. J Chem Phys 117(16):7433–7447

29. Marques MAL, Gross EKU (2004) Time-dependent density functional theory. Annu Rev Phys Chem 55:427–455

30. Yanai T, Tew DP, Handy NC (2004) A new hybrid exchange-correlation functional using the Coulomb-attenuating method (CAM-B3LYP). Chem Phys Lett 393(1–3):51–57

31. Stephens PJ, Devlin FJ, Chabalowski CF, Frisch MJ (1994) Ab initio calculation of vibrational absorption and circular dichroism spectra using density functional force fields. J Phys Chem 98(45):11623–11627

32. Cheol HC, Miklos K, Alfred K (1997) Limitations of current density functional theories for the description of partial pi-bond breaking. Chem Phys Lett 276(3–4):266–268

33. Chai JD, Head-Gordon M (2008) Systematic optimization of long-range corrected hybrid density functionals. J Chem Phys 128(8):084106

34. Rostov IV, Amos RD, Kobayashi R, Scalmani G, Frisch MJ (2010) Studies of the ground and excited-state surfaces of the retinal chromophore using CAM-B3LYP. J Phys Chem B 114(16):5547–5555

35. Rostov IV, Kobayashi R, Amos RD (2012) Comparing long-range corrected functionals in the cis–trans isomerisation of the retinal chromophore. Mol Phys 110(19–20):2329–2336

36. Zhao Y, Truhlar DG (2008) Density functionals with broad applicability in chemistry. Acc Chem Res 41(2):157–167

37. Scalmani G, Frisch MJ, Mennucci B, Tomasi J, Cammi R, Barone V (2006) Geometries and properties of excited states in the gas phase and in solution: theory and application of a time-dependent density functional theory polarizable continuum model. J Chem Phys 124(9):094107

38. Hirata S, Head-Gordon M (1999) Time-dependent density functional theory within the Tamm–Dancoff approximation. Chem Phys Lett 314(3–4):291–299

39. Frisch MJ, Trucks GW, Schlegel HB, Scuseria GE, Robb MA, Cheeseman JR, Scalmani G, Barone V, Mennucci B, Petersson GA, Nakatsuji H, Caricato M, Li X, Hratchian HP, Izmaylov AF, Bloino J, Zheng G, Sonnenberg JL, Hada M, Ehara M, Toyota K, Fukuda R, Hasegawa J, Ishida M, Nakajima T, Honda Y, Kitao O, Nakai H, Vreven T, Montgomery JA, Peralta JE, Ogliaro F, Bearpark M, Heyd JJ, Brothers E, Kudin KN, Staroverov VN, Kobayashi R, Normand J, Raghavachari K, Rendell A, Burant JC, Iyengar SS, Tomasi J, Cossi M, Rega N, Millam JM, Klene M, Knox JE, Cross JB, Bakken V, Adamo C, Jaramillo J, Gomperts R, Stratmann RE, Yazyev O, Austin AJ, Cammi R, Pomelli C, Ochterski JW, Martin RL, Morokuma K, Zakrzewski VG, Voth GA, Salvador P, Dannenberg JJ, Dapprich S, Daniels AD, Farkas, Foresman JB, Ortiz JV, Cioslowski J, Fox DJ (2009) Gaussian 09, Revision C.01, Wallingford, CT

40. Klok M, Walko M, Geertsema EM, Ruangsupapichat N, Kistemaker JCM, Meetsma A, Feringa BL (2008) New mechanistic insight in the thermal Helix inversion of second-generation molecular motors. Chem Eur J 14(35):11183–11193